Developing thermodynamic stability diagrams for equilibrium-grain-size binary alloys

Naixie Zhou, Jian Luo *

Department of NanoEngineering, Program of Materials Science and Engineering, University of California, San Diego; La Jolla, CA 92093-0448, USA

ARTICLE INFO

ABSTRACT

Bulk computational thermodynamics are extended to model binary poly/nanocrystalline alloys by incorporating grain boundary energies computed by a multilayer adsorption model. A new kind of stability diagram for equilibrium-grain-size poly/nanocrystalline alloys is developed. Computed results for Zr-doped Fe are validated by prior experiments and provide new physical insights regarding stabilization of nanoalloys and its relation to solid-state amorphization. This work supports a major scientific goal of extending bulk computational thermodynamics methods to interfaces and nanomaterials and developing relevant thermodynamic stability diagrams as extensions to bulk phase diagrams, which can be useful new tools for the "Materials Genome" initiative.

1. Introduction

In 1993, Weissmüller [1,2] reported a theory of thermodynamic stabilization of nanocrystalline alloys, and this theory was further elaborated by Kirchheim et al. [3,4]. It was proposed that the thermodynamic driving force for grain growth can be reduced by reducing GB energy (γ_{GB}) via GB segregation (*a.k.a.* adsorption). A nanocrystalline alloy can be stabilized as the effective γ_{GB} approaches zero. Subsequent experiments have been conducted to seek for stabilized nanocrystalline alloys in Fe–Zr [5,6], Pd–Zr [7], and other systems [8–10]. In these systems, the "stable" nanocrystalline alloys typically represent *metastable states* in supersaturated regions occurring when precipitation is hindered kinetically. This is consistent with Kirchheim's analysis [3]. Recently, Schuh and co-workers developed a "Regular Nanocrystalline Alloy" model and analyzed systems with positive pair-interaction parameters [11–13]. Saber et al. refined this model by incorporating both chemical and elastic segregation enthalpies [14], which was also an extension of their earlier model of ferrous alloys [15]; both models used a simplified monolayer/bilayer version of the Wynblatt–Ku type segregation formulation [16]. This work further combines a calculation of phase diagrams (CALPHAD) analysis with a more realistic Wynblatt–Chatain type multilayer segregation (complexion) model [16] to simulate stable, metastable and unstable regions of polycrystalline binary alloys systematically for multiple phase fields, providing new quantitative insights regarding the competitions and underlying relations among precipitation, stabilization of nanoalloys, and solid-state amorphization.

A further scientific goal of this study is to develop new thermodynamic stability diagrams (as extensions to bulk phase diagrams) as novel materials design tools. In a boarder content, phase diagrams, along with CALPHAD methods [17], are arguably amongst the most useful tools for materials design. It is now well-established that the thermodynamic stability of an interface or a nanoscale system that has a large amount of interfaces can drastically differ from that of a bulk material. As an example, nanoparticles can often melt at hundreds of degrees below the bulk melting temperature [18]; along this line, Tanaka et al. extended CALPHAD methods to compute phase diagrams for nanoparticles of binary alloys [19,20]. In another relevant study, researchers demonstrated that nanometer-thick, impurity-based, liquid-like films can be stabilized at grain boundaries (GBs) well below the bulk solidus lines [21–23]. Further studies extended the bulk CALPHAD methods to predict the stability of such liquid-like intergranular films (which can be considered as an "interfacial phase" and named as "complexion" to differentiate them from bulk phases [24–29]) and such GB diagrams are proven useful for forecasting activated sintering and designing sintering protocols [30–33]. This series of recent studies collectively point us to a potentially-transformative research direction of extending bulk CALPHAD methods to interfaces and nanomaterials with a large amount of interfaces; some research efforts in this area are also reviewed by Kaptay [34]. This work represents another such new endeavor of modeling equilibrium-grain-size poly/nanocrystalline alloys by incorporating GB energies in thermodynamic modeling.

It is important to differentiate two possible types of thermodynamic stability diagrams that may be developed for nanomaterials.

* Corresponding author. Tel.: +1 858 246 1203; fax: +1 858 534 9553.
E-mail address: jluo@alum.mit.edu (J. Luo).

The first type of diagrams represent the shifts in phase boundaries given a constraint of artificially-fixed sizes (e.g., particle or grain sizes); Tanaka et al.'s studies of binary nanoparticles [19,20] belong to this type. The current study aims to develop the second type of stability diagrams to model the thermodynamic stability of equilibrium-grain-size poly/nanocrystalline alloys without imposing pre-selected (kinetically-determined) grain sizes. Fe–Zr is selected as our modeling system because of the existence of both thermodynamic data [35] and experimental results [5,6,36], and our goal is to develop models and methods that can be extended to other systems. In the current (first) study, we model a binary poly/nanocrystalline alloy (of equiaxed grains) for which experimental data exist for validation. Our ultimate goal is to further extend the methods to multicomponent alloys, where they can have more impacts (similar to bulk CALPHAD methods).

2. Modeling methods

At constant pressure and temperature, the molar free energy of a polycrystalline binary alloy A–B (A=Fe and B=Zr for our specific case) can be written as

$$G_m = (1-X)\mu_A + X\mu_B + \overline{A_{GB}}\gamma_{GB}, \tag{1}$$

where X is the overall composition (atomic fraction) of the solute B, μ_A and μ_B are chemical potentials, $\overline{A_{GB}}$ is the GB area per mole of atoms, and γ_{GB} is the GB energy. When the grain size is small, the overall composition (X) differs from the bulk/crystal composition (X_C, inside the grain) because of GB segregation; the mass conservation law specifies

$$X \approx X_C + \overline{A_{GB}}\Gamma, \tag{2}$$

where Γ is the GB excess of solute. Recent observations of the increased apparent solubility of dopants in nanocrystalline ZnO [37] and steels [38,39] are likely due to that X can be substantially greater than X_C for nano-grained materials. Under the condition of a kinetically-limited (fixed) grain size, the changed solubility can also be partially related to a shift in the X_C value (in equilibrium with the secondary phase) due to the added $\overline{A_{GB}}\gamma_{GB}$ term in Eq. (1); this effect should be modeled by the first type of stability diagrams (with per-selected grain sizes) discussed above, which is beyond the scope of this letter.

In this study, we adapt the Wynblatt–Chatain multilayer segregation (complexion) model [16] to consider general twist GBs in a BCC alloy; the following expression is derived by adapting the Wynblatt–Chatain equations [16] (with two modifications: we assume $J_{max}=1$ or all broken bonds exist in the first layer since we adopt a general twist (110) GB to represent the general GBs in Fe; we also adjusted the in-plane and vertical coordinate numbers since the original Wynblatt–Chatain model is for FCC alloys):

$$\gamma_{GB} = \min\Bigg\{(p-1)z_v N \Big[2X_{GB}^1(1-X_{GB}^1)\omega + X_{GB}^1 e_{BB} + (1-X_{GB}^1)e_{AA}\Big]$$

$$-2N\sum_{i=1}^{+\infty}\Big[X_{GB}^i \Delta E_{els}^i\Big] + 2N\omega\sum_{i=1}^{+\infty}\Big[-z(X_{GB}^i - X_C)^2 + z_v(X_{GB}^i - X_{GB}^{i+1})^2\Big]$$

$$+2NkT\sum_{i=1}^{+\infty}\Big[X_{GB}^i \ln\Big(\frac{X_{GB}^i}{X_C}\Big) + (1-X_{GB}^i)\ln\Big(\frac{1-X_{GB}^i}{1-X_C}\Big)\Big]\Bigg\}, \tag{3}$$

where X_{GB}^i is the composition in the ith layer near the GB core, e_{AA}, e_{BB}, and e_{AB} are bonding energies ($e_{FeFe} = -1.07$ eV/bond and $e_{ZrZr} = -1.56$ eV/bond, which are estimated from atomization enthalpies [40]. The energy difference between the HCP and BCC phase for Zr is corrected by using CALPHAD data [35], ω [$\equiv e_{AB} - 0.5(e_{AA} + e_{BB})$] is the pair-interaction parameter (estimated to be -0.025 eV/bond for Fe–Zr from the CALPHAD

data [35]), z is the total coordination number ($z=8$ for BCC), z_v is the coordination number above the plane ($z_v=2$ for a BCC twist (110) GB), p (the fraction of reconnected bonds) is set to be 5/6 to represent a "general GB" so that the GB energy is 1/3 of the surface energy for a pure element, N is the number of the lattice sites per unit area, k is the Boltzmann constant and T is temperature. ΔE_{els}^i is the elastic energy in the ith layer, which decreases exponentially with the distance to the GB core (h^i) according to $\Delta E_{els}^i = \Delta E_{els}^1 \exp[-1.01(h^i/r_B)^{1.53}]$, where r_B is the atomic radius of B; ΔE_{els}^1 is given by the Friedel model [16], which is calculated to be 0.96 eV/atom for Fe–Zr. The equilibrium GB adsorption profile can be obtained by minimizing Eq. (3) ($\partial\gamma_{GB}/\partial X_{GB}^i = 0$), leading to a McLean type adsorption equation for each layer:

$$\frac{X_{GB}^i}{1-X_{GB}^i} = \frac{X_C}{1-X_C}\exp\left(-\frac{\Delta H_{seg}^i}{RT}\right) \tag{4}$$

Here, ΔH_{seg}^i is the adsorption enthalpy of the ith layer and its specific expression is given in Ref. [16]. Eqs. (3) and (4), along with the adsorption profile ($X_{GB}^i)_{i=1, 2,...}$ that minimizes Eq. (3), can be solved efficiently via an iterative method. The GB excess of solute is given by $\Gamma \approx 2N\sum_i(X_{GB}^i - X_C)$.

3. Results and discussion

Fig. 1 shows several computed normalized GB energy ($\gamma_{GB}/\gamma_{GB}^{(0)}$) and GB excess of solute (Γ) vs. bulk composition (X_C) curves. Here, $\gamma_{GB}^{(0)}$, the GB energy for pure Fe, is computed from Eq. (3) to be ~ 1 J/m^2, which is consistent with the measured value [41]. In a binary alloy, GB adsorption reduces GB energy according to
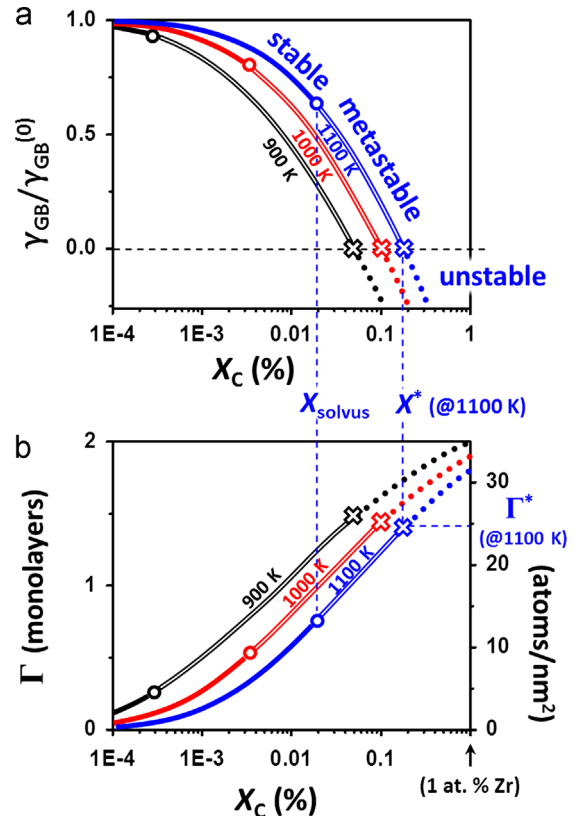

Fig. 1. Computed (a) normalized GB energy ($\gamma_{GB}/\gamma_{GB}^{(0)}$) and (b) GB excess of the solute (Γ) vs. bulk composition (X_C) curves for Zr-doped Fe. The stable, metastable, and unstable regions, respectively, are represented by the solid, double, and dotted lines, respectively.

the Gibbs isothermal: $d\gamma_{GB} = -\Gamma_A\, d\mu_A - \Gamma_B\, d\mu_B \approx -\Gamma\, d(\mu_B - \mu_A)$. The double lines in Figs. 1 and 2 represent metastable states ($X_C > X_{soluvs}$) occurring when the precipitation is hindered.

We use X^*, Γ^*, μ^*_A, and μ^*_B to denote the conditions that the effective γ_{GB} is reduced to 0, which are labeled by the open crosses in Figs. 1 and 2. Beyond this point ($X_C > X^*$), a negative γ_{GB} represents an unstable state (indicated by dotted lines in Figs. 1 and 2), which should lead to a spontaneous increase in the GB area ($\overline{A_{GB}}$) with solute segregation that decreases X_C to a fixed value of X for a closed system. Consequently, an *equilibrium* grain size can be achieved with the effective γ_{GB} being kept at ~ 0 [3,4,8]. This equilibrium grain size can be estimated by plugging X^* and Γ^* into Eq. (2) and adopting an approximation for grain size

for equiaxed grains ($d \approx 3\overline{V}\,/\,\overline{A_{GB}}$, where $\overline{V}$ is the molar volume), as

$$d_{eq} \approx \frac{3\overline{V}\Gamma^*}{X - X^*} \tag{5}$$

Rewriting Eq. (1) for the polycrystalline alloy with an equilibrium grain size ($\gamma_{GB} = 0$) produces

$$G_m(\text{eq.-grain-size alloy}) = (1-X)\mu^*_A + X\mu^*_B \tag{6}$$

The free-energy curve for this equilibrium-grain-size alloy is represented by the purple double line in Fig. 2, which is a tangent line that touches the free-energy curve of the A-rich α phase at X^*; with increasing X, this alloy exhibits a decreasing equilibrium grain size (proportional to $1/(X-X^*)$) and this line ends at a solid-state amorphization limit, which corresponds to the condition that d_{eq} approaches the atomic size.

In this study, we combine the Wynblatt–Chatain multilayer GB segregation (complexion) model [16] with an analysis for the Fe–Zr binary system [35]. To systematically represent the computed results, we plot lines of constant normalized GB energies and equilibrium grain sizes in the bulk phase diagram in Fig. 3 for the Zr-doped Fe system.

As shown in Fig. 3, GB segregation reduces γ_{GB} (the driving force of grain growth) systematically. Beyond the solvus line, γ_{GB} can be further reduced if the precipitation of the secondary phase ($Fe_{23}Zr_6$ etc.) is kinetically hindered; these metastable states are represented by dashed lines in Fig. 3. The effective γ_{GB} vanishes at $X = X^*$ (≈ 0.002 at.% at ~ 600 K and ≈ 0.2 at.% at $T_{eutectoid}$, as shown in Fig. 3). Beyond this line, a metastable polycrystalline alloy with an equilibrium grain size has lower energies than those of the unstable BCC phase (as schematically illustrated in Fig. 2), and computed equilibrium grain sizes (using Eq. (5)) are plotted in Fig. 3. For a strong segregation system (like Fe–Zr) where X is small and Γ is almost a constant (Fig. 1), the temperature-dependence of d_{eq} becomes insignificant in the nano-region ($d_{eq} < 100$ nm) according to Eq. (5); a more significant temperature-dependence is expected for a weaker segregation system. We should emphasize that these dashed lines in Fig. 3 represent the metastable states only
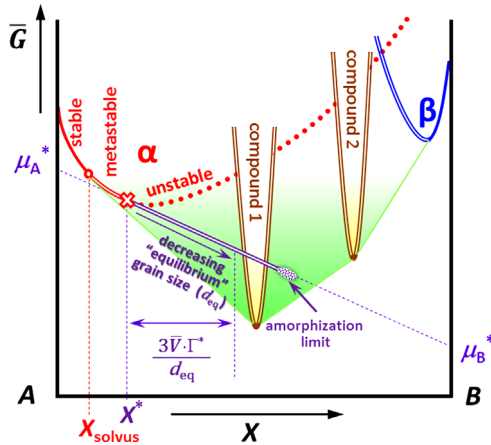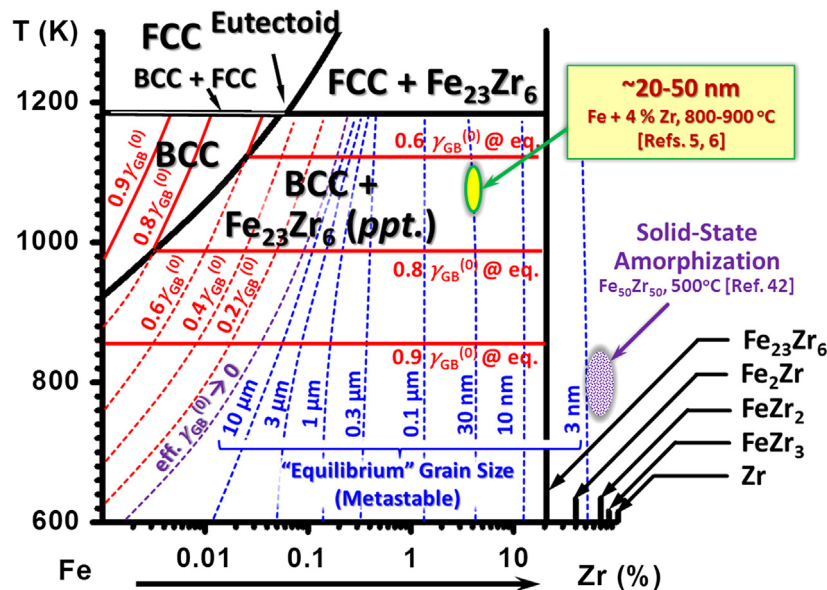

Fig. 2. Schematic illustration of molar free energy vs. composition curves for a binary A–B alloy. If the precipitation of the B-enriched secondary phase(s) is kinetically hindered, a metastable α phase can form at $X > X_{soluvs}$ (represented by the red double line); the metastable α phase becomes unstable at $X > X^*$ (represented by the red dotted line); in this region, a metastable polycrystalline alloy will form with an "equilibrium" grain size (d_{eq}), which is represented by a tangent line that starts at $X = X^*$; for this equilibrium-grain-size alloy, d_{eq} is inversely proportional to (X–X^*), and this line ends at an amorphization limit when d_{eq} approaches the atomic size. (For interpretation of the reference to color in this figure, the reader is referred to the web version of this article)

Fig. 3. Computed lines of constant normalized GB energies and *equilibrium* grain sizes are plotted in the bulk phase diagram of Fe–Zr; the x-axis represents logarithmical overall composition (atomic percentage of Zr) and only two phase fields are completely shown. The equilibrium states are represented by solid lines and the metastable states are represented by dashed lines. The bulk phase diagram was also computed; the BCC and FCC two-phase region is very narrow so that the two phase boundary lines appear to overlap at this scale. Noting that the composition is plotted in logarithmical scale so that the computed solvus line intersects with (instead of asymptotically approaching) the temperature axis.

under the conditions that the precipitation is hindered; if the precipitation of $Fe_{23}Zr_6$ is allowed, the three horizontal lines in the two-phase region of Fig. 3 represent the true equilibrium states.

The bulk phase diagram shown in Fig. 3 was computed using the bulk CALPHAD data from Ref. [35]. In this case, there is no shift in the bulk phase boundaries at the thermodynamic equilibria (because the equilibrium grain size is infinity at all equilibrium bulk phase boundaries). It is important to note that this case is different from prior studies of modeling nanoparticles with pre-selected particle sizes [19,20].

The computed Fig. 3 compares favorably with two independent sets of prior experiments. Darling et al. reported that a Fe+4 at% Zr alloy made by high-energy ball milling exhibited a "stable" XRD grain size of 20–30 nm after annealing at 800 °C [6]; later they also showed that a TEM grain size of ~52 nm was retained in a ball milled Fe+4 at% Zr nanoalloy after annealing at 900 °C [5]. This is consistent with the computed result of ~30 nm at this condition (Fig. 3). The computed Fig. 3 also suggests an amorphization limit at ~50% of Zr. This is also consistent with the solid-state amorphization of $Fe_{50}Zr_{50}$ multilayers reported in another prior study [42]; this agreement not only supports our model but also reveals the underlying relation between two phenomena – stabilization of nanocrystalline alloys and solid-state amorphization – both occurring in the Fe–Zr system only if the precipitation is kinetically hindered (even though we recognize the existence of a more accurate model for solid-state amorphization [36]).

4. Conclusions

In summary, we have extended bulk computational thermo-dynamic methods to model binary equilibrium-grain-size poly/ nanocrystalline alloys by incorporating GB energies computed by a Wynblatt–Chatain multilayer GB complexion model [16]. This letter also reports a framework to combine a bulk CALPHAD analysis with a GB segregation (complexion) model using an explicit (simple) approach. In future studies, new interfacial thermodynamic models that consider complex GB complexions [24–29] beyond the classical GB segregation types can be further developed and incorporated. A key contribution of the current study is the development of a new kind of thermodynamic stability diagrams equilibrium-grain-size alloys. In particular, a new stability diagram is computed for Zr-doped Fe (as our model system) and validated with multiple prior experiments. In addition to earlier studies of developing phase diagrams for binary nanoparticles [21–23] and GB diagrams [30–33], the success of this study represents a further step towards realizing a major scientific goal of developing stability diagrams for interfaces and nanoscale systems as extensions of bulk phase diagrams, which can be used as general tools to accelerate materials design in the spirit of the "Materials Genome" initiative.

References

[1] Weissmuller J. J Nanostruct Mater 1993;3:261.
[2] Weissmuller J. J Mater Res 1994;9:4–7.
[3] Kirchheim R. Acta Mater 2002;50:413–9.
[4] Liu F, Kirchheim R. J Cryst Growth 2004;264:385–91.
[5] Darling KA, VanLeeuwen BK, Koch CC, Scattergood RO. Mater Sci Eng A 2010;527:3572–80.
[6] Darling KA, Chan RN, Wong PZ, Semones JE, Scattergood RO, Koch CC. Scr Mater 2008;59:530–3.
[7] VanLeeuwen BK, Darling KA, Koch CC, Scattergood RO, Butler BG. Acta Mater 2010;58:4292–7.
[8] Krill CE, Ehrhardt H, Birringer R. Z Metallkd 2005;96:1134–41.
[9] Koch CC, Scattergood RO, Darling KA, Semones JE. J Mater Sci 2008;43: 7264–7272.
[10] Koch CC. J.Mater Sci 2007;42:1403–14.
[11] Trelewicz JR, Schuh CA. Phys Rev B 2009;79.
[12] Chookajorn T, Murdoch HA, Schuh CA. Science 2012;337:951–4.
[13] Murdoch HA, Schuh CA. Acta Mater 2013;61:2121–32.
[14] Saber M, Kotan H, Koch CC, Scattergood RO. J. Appl Phys 2013;113:063515.
[15] Darling KA, VanLeeuwen BK, Semones JE, Koch CC, Scattergood RO, Kecskes LJ, et al. Mater Sci Eng A 2011;528:4365–71.
[16] Wynblatt P, Chatain D. Metall Mater Trans A 2006;37A:2595–620.
[17] Kattner UR. J Met 1997;49:14–9.
[18] Mei QS, Lu K. Prog Mater Sci 2007;52:1175–262.
[19] Tanaka T, Hara S. Z Metallkd 2001;92:467–72.
[20] Tanaka T, Hara S. Z Metallkd 2001;92:1236–41.
[21] Luo J, Gupta VK, Yoon DH, Meyer HM. Appl Phys Lett 2005;87:231902.
[22] Luo J. Crit Rev Solid State Mater Sci 2007;32:67–109.
[23] Shi X, Luo J. Appl Phys Lett 2009;94:251908.
[24] Dillon SJ, Tang M, Carter WC, Harmer MP. Acta Mater 2007;55:6208–18.
[25] Harmer MP. J Am Ceram Soc 2010;93:301–17.
[26] Harmer MP. Science 2011;332:182–3.
[27] Luo J., Cheng H., Asl K.M, Kiely C.J, Harmer M.P. Science. 2011;333:1730-1733.
[28] Tang M, Carter WC, Cannon RM. Phys Rev B 2006;73:024102.
[29] Kaplan WD, Chatain D, Wynblatt P, Carter WC. J.Mater Sci 2013;48:5681–717.
[30] Luo J. Curr Opin Solid State Mater Sci. 2008;12:81–8.
[31] Luo J, Shi XM. Appl Phys Lett 2008;92:101901.
[32] Shi X, Luo J. Phys Rev B 2011;84:014105.
[33] Luo J. J Am Ceram Soc 2012;95:2358–71.
[34] Kaptay GJ. Mater Sci 2012;47:8320–35.
[35] Servat C, Gueneau C, Ansara I. J Alloys Compd 1995;220:19–26.
[36] Liu BX, Lai WS, Zhang ZJ. Adv Phys 2001;50:367–420.
[37] Straumal BB, Protasova SG, Mazilkin AA, Schütz G, Goering E, Baretzky B, et al. JETP Lett 2013;97:367–77.
[38] Straumal BB, Mazilkin AA, Protasova SG, Myatiev AA, Straumal PB, Baretzky B. Acta Mater 2008;56:6246–56.
[39] Straumal BB, Dobatkin SV, Rodin AO, Protasova SG, Mazilkin AA, Goll D, et al. Adv Eng Mater 2011;13:463–9.
[40] Cox JD, Wagman D, Medvedev VA. CODATA Key values for thermodynamics. Hemisphere Publishing Corp; 1989.
[41] Roth TA. Mater Sci Eng A 1975;18:183–92.
[42] Paesano A, Teixeira SR, Amarai L. Hyperfine Interact 1991;67:665–9.